Open Ceramics 23 (2025) 100818

Contents lists available at ScienceDirect

Open Ceramics

journal homepage: www.sciencedirect.com/journal/open-ceramics

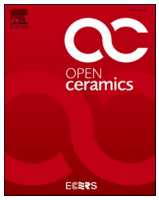

Dielectric property measurement of a SiC_f/SiC ceramic matrix composite via microwave cavity characterisation

Jordan Stephen [a], Spencer Jeffs [a,*], Heungjae Choi [b], Adrian Porch [b]

[a] Institute of Structural Materials, Faculty of Science & Engineering, Swansea University, SA1 8EN, UK
[b] Centre for High Frequency Engineering, School of Engineering, Cardiff University, CF24 3AA, UK

ARTICLE INFO

Keywords:
Ceramic matrix composites
Dielectric properties
Microwave cavity characterisation

ABSTRACT

Ceramic Matrix Composites (CMCs) are used for high temperature structural engineering applications, such as those found within gas turbine engines. When operating in these environments they can undergo oxidation and damage that may not be easily detectable, emphasising the need for a non-invasive assessment approach that could detect such changes. In this research, we use a single mode microwave cavity for sensitive dielectric property measurement as a method of assessment for Silicon Carbide (SiC) CMC material. We have also used this method to characterise individual bundles of SiC fibres, to develop an understanding of the method. Environmental conditions are then applied to the CMC samples including a high temperature exposure at 800 °C, and humidity exposures followed by two different 800 °C reheat durations. Characterisation was performed on the pre- and post-exposed material to verify the severity of each exposure, both microstructurally and mechanically, to compare these with microwave dielectric property data.

1. Introduction

1.1. Ceramic matrix composites (CMCs)

CMCs offer a variety of performance advantages over many current metallic alloy systems when used for high temperature component applications, like those found within the hottest sections of the gas turbine engine. They provide a combination of excellent thermal stability coupled with low density, resulting in great potential for improving fuel efficiency, reducing emissions, and decreasing the need for additional cooling requirements within the engine [1].

Unlike conventional monolithic ceramics, CMCs can provide these benefits without sacrificing considerable toughness and damage tolerance, maintaining a non-linear stress-strain response as a result. This non-linear response is largely credited to the ability of the reinforcing fibres to bridge and deflect non-critical transverse matrix cracks, enabling the material to absorb additional energy before fracture. This ability relies heavily on a well-designed interphase layer between the fibres and the matrix. Boron nitride and carbon-containing interphases are often used to supply the 'weak' interfacial bond necessary for damage to propagate around the fibres, resulting in larger crack openings and the ability to carry non-linear strain before failure [2].

Silicon carbide (SiC) CMCs (specifically SiC_f/SiC) have shown great promise for extended high temperature applications in oxidising environments and are being developed for use in several non-critical gas turbine components, due to a density approximately two thirds less than that of currently used nickel-based superalloys. This provides significant opportunities for weight reduction in the hotter sections, where temperatures exceed 800 °C [3]. However, there remains uncertainty around the exact nature of oxidation, damage, and failure mechanisms when subjected to these extreme mechanical and environmental conditions over long periods. This has resulted in the need to develop reliable damage monitoring and assessment techniques such as acoustic emission (AE), electrical resistance (ER), and digital image correlation (DIC) [4–7], typically implemented during mechanical loading. In addition, techniques such as X-ray computed tomography (XCT) [8,9] and vibration [10,11] have been applied to understand and assess the condition of CMC materials.

1.2. Damage in CMCs

The initiation and progression of damage in CMCs is dictated by several mechanisms that eventually result in global fracture of components. These mechanisms include matrix cracking, interface debonding,

* Corresponding author.
E-mail address: s.p.jeffs@swansea.ac.uk (S. Jeffs).

https://doi.org/10.1016/j.oceram.2025.100818
Received 10 April 2025; Received in revised form 3 June 2025; Accepted 24 June 2025
Available online 25 June 2025

delamination, fibre pull-out and fibre fracture [12]. For 2D CMCs, matrix cracks typically form at small voids or inclusions within the 90° plies and propagate via a three-dimensional tunnelling process above a specific matrix cracking onset stress [13]. These cracks reduce the material's stiffness and induce permanent strain on the system [14]. The cracks extend laterally towards the 0° plies, where fibre debonding and sliding result in additional permanent inelastic strain. In addition, these cracks, along with any small voids or inclusions, provide a pathway for internal oxidation and degradation of the interphase layer at higher temperatures, causing embrittlement of the composite and compromising its desired mechanical response. As the matrix becomes saturated with cracks, the fibres in the 0° tows are forced to sustain the majority of the load, with only a small amount of stress redistribution due to the friction between the de-bonded matrix and fibres. This is followed by localised fibre fracture and eventually global failure.

Oxidation of the interphase layer is a potential limiting factor associated with using SiC_f/SiC CMCs for high temperature gas turbine applications. The thin interphase layer used to promote fibre-matrix debonding typically degrades under oxidation conditions leaving behind brittle glass-like phase if not appropriately protected [15]. Permissible cracks and voids within the material provide hot gas paths for volatile vapour phases, allowing moisture to attack and degrade the interphase layer [16]. The resultant silica formation on the fibres in the absence of the interphase layer can result in fusion of both fibre to fibre and fibre to matrix. Even a small amount of bonding caused by oxidation can eliminate the ability of fibres to act independently, removing the primary toughening mechanism within the composite. Therefore, there is interest in developing the ability to easily detect these types of environmental degradation through non-invasive assessment.

1.3. Electromagnetic tests of damage in CMCs

Various Electromagnetic (EM) techniques have been proposed to assess damage propagation and accumulation of CMCs, examples including the free space reflection/transmission of EM waves [17] and impedance spectroscopy [18,19]. Changes in the dielectric or conducting properties are used as indicators of a sample's damage state, assuming that the sample geometry is unaffected. Free space methods are non-contacting and non-invasive but require a sophisticated experimental set-up involving an antenna range, with samples restricted to thin sheets of large areas unless operated at mm-wave frequencies (e.g. above 30 GHz). Impedance spectroscopy measurements use smaller samples (typically of area < 1 cm^2) but the method requires metal contacts which can introduce large systematic errors in the measurements.

In this paper we use a resonant microwave cavity, into which the sample can be easily inserted and removed, for its dielectric property characterisation using the cavity perturbation method [20]. This method is well-established, and its attractiveness arises from it being non-invasive, non-destructive, highly sensitive, volumetric, simple, fast (data acquisition rates can exceed 1 kHz), with no need for specific sample geometries. Here, we use the same standard CMC samples for mechanical testing for the microwave cavity characterisations. The host cavity can be designed (via its size and shape) to operate at any frequency within the microwave spectrum (1 GHz – 30 GHz) and here we use a frequency of 2.5 GHz, pulled down to 2.4 GHz by a standard CMC sample. The reason for this choice is twofold; firstly, 2.4 GHz – 2.5 GHz has been allocated as an industrial, scientific and medical (ISM) radio band, reserved for purposes other than telecommunications, and is used commonly for microwave materials processing (as in the ubiquitous domestic microwave oven); secondly, at this frequency the microwave fields will fully penetrate the standard CMC sample and so we obtain volumetric (rather than surface) dielectric characterisation. The cavity perturbation method involves the measurement of changes in resonant frequency, f, and quality factor, Q, associated the sample. At microwave frequencies we express a material's relative permittivity as the complex quantity $\varepsilon = \varepsilon_1 - j\varepsilon_2$, where $\varepsilon_1 - 1$ quantifies its polarisation (from decreases in f) and ε_2 its dielectric loss (from reduction in Q, i.e. increases in $1/Q$), respectively, in response to the applied electric field. For conducting samples (such as SiC fibres), the loss term ε_2 can be used to calculate the electrical conductivity. The dielectric property changes when a CMC sample undergoes environmental degradation can be measured precisely and unambiguously using the cavity perturbation method, without the need for complicated data analysis.

1.4. Synopsis of the paper

The paper is arranged as follows. After having introduced CMCs and the importance of environmental degradation detection, we next review the microwave cavity perturbation technique and its application to the dielectric property measurements of the CMC samples studied here. We then demonstrate the importance of sample orientation, first via dielectric characterisation of identically shaped polylactic acid (PLA) samples (whose analysis is assisted by finite element modelling), then via measurements of SiC fibres. The SiC fibre measurements demonstrate the extreme anisotropy of microwave loss, which is very high when the electric field is applied parallel to the fibres (owing to their high electrical conductivity) but negligible when applied perpendicular (owing to electric field depolarisation). Crucially, this means in the perpendicular orientation the microwave loss of the CMC material becomes sensitive to the material outside of the fibres, rather than the fibres themselves, which is the sample region susceptible to environmental damage. We then apply a series of CMC samples to a range of systematic heat and humidity exposures, followed by mechanical, microstructural and microwave characterisation. This allows us to validate the measurements of microwave dielectric property (with the microwave E-field applied perpendicular to the length of the CMC) as a viable method of assessing environmental degradation in these CMC samples.

2. Materials and methods

2.1. Standard CMC samples for mechanical and microwave testing

The samples used in this research are SiC_f/SiC CMC samples that were manufactured at Rolls-Royce High Temperature Composites Inc (California, USA) via a proprietary processing route. Each sample was machined from a larger CMC panel of ~152 × 100 mm. The panels consist of two-dimensionally woven Hi-Nicalon™ SiC fibre bundles (NGS Advanced Fibres Co, Japan) orientated at 0 and 90° to form a five-harness satin (5HS) weave, with a panel containing 18 plies providing a thickness of approximately 5 mm. The woven fibre preforms are coated with a boron nitride (BN) interphase layer via chemical vapour infiltration (CVI) and partially densified with SiC using the same process. The final matrix was obtained via the slurry infiltration of SiC particles and melt infiltration with silicon [21]. An example of an as-received SiC_f/SiC CMC sample can be seen in Fig. 1. Each sample is approximately 152 mm in length with a narrower 50 mm long, 9 mm wide central gauge section that has a cross-sectional area of approximately 45mm^2.

The corresponding microstructure can be seen in Fig. 2a. This consists of 0° fibre tows that run horizontally across the image, spanning the entire length of the sample, and 90° tows that have been sectioned and appear head on. Each fibre tow is approximately 1000 μm wide and contains approximately 500 reinforcing fibres per bundle. Individual SiC

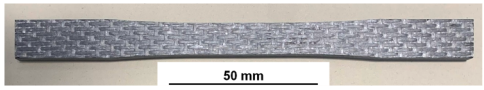

Fig. 1. As received SiC_f/SiC CMC sample.

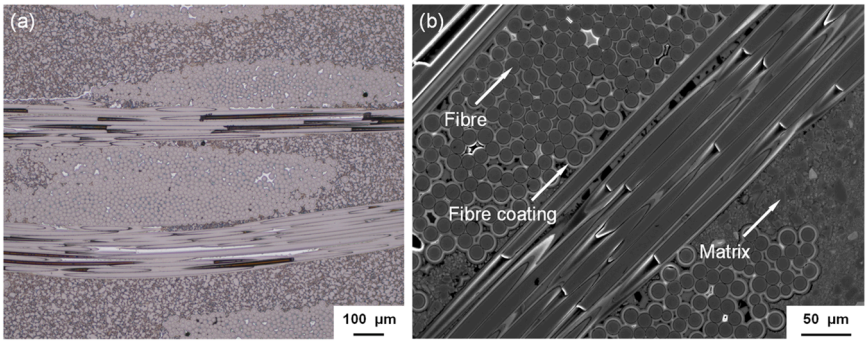

Fig. 2. As-received SiC_f/SiC CMC microstructure.

fibres can be identified as the light grey circles that occupy a large portion of the micrograph. Each fibre has a diameter of approximately 10 μm and is coated with a submicrometer boron nitride (BN) interphase layer that provides chemical resistance and enhanced toughness by acting as the weak mechanical interface between the fibres and the matrix. Scanning electron microscope (SEM) imaging was used to further characterise the microstructure at high magnification Fig. 2b The BN interphase layer can be identified as the dark band that surrounds each individual fibre. The BN interphase layer is surrounded by CVI SiC that protects the boron nitride phase from degradation during the melt infiltration (MI) processes used for the matrix phase [22]. SiC particles contained within the MI matrix can be identified as the grey granular sections whereas the MI silicon phase appears as the brighter sections due to its greater density.

2.2. Microwave host cavity and microwave measurements

The dielectric properties of all SiC_f/SiC samples are characterised via their perturbations of a cylindrical aluminium cavity, resonating in its TM_{010} mode at 2.5 GHz when empty, which has been applied previously for dielectric characterisation of a range of other materials [23–25].

The electromagnetic (EM) fields of the TM_{010} mode of a regular cylindrical cavity are shown schematically in Fig. 3; the electric (E) and magnetic (H) fields shown are 90° out of phase with each other in the time domain and resonance is associated with the exchange of EM field energy between these two states at the resonant frequency. The TM_{010} mode is chosen owing to its well-defined E-field distribution, into which the sample is inserted. As for any resonant system (electrical or mechanical), the quality factor Q is defined as 2π times the fraction of energy stored to energy lost per cycle, so $1/Q$ quantifies the total loss. For the TM_{010} mode to have a resonant frequency of 2.5 GHz when empty, we design [26] the cavity to have an internal height $d = 40$ mm

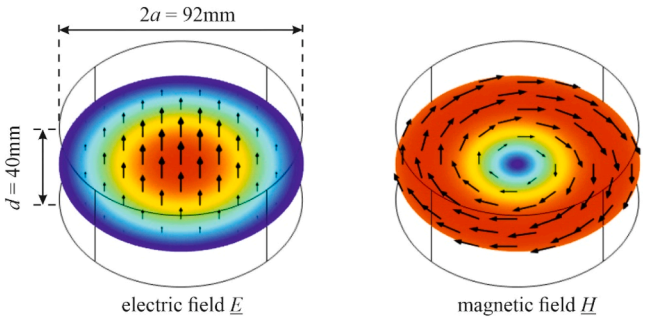

Fig. 3. The electric and magnetic field distributions of the TM_{010} resonant mode of a cylindrical cavity, at 2.50 GHz for the internal dimensions shown. Note that there is no height variation of either field in this mode, so the same field patterns are produced for every slice taken perpendicular to the cavity axis.

and internal radius $a = 46$ mm and the practical cavity is CNC machined from bulk aluminium metal. Although the TM_{010} resonant frequency does not depend on the internal height d [26], this must be chosen wisely. Our choice of $d/a = 0.87$ is a compromise between good spectral separation of resonant modes (the TE_{111} mode is then at 4.21 GHz and the closest mode to TM_{010} is TM_{110} at 3.98 GHz) and high Q, preserving 53 % of the maximum Q factor attained in the hypothetical limit when d/a tends to infinity. The measured resonant frequency of the TM_{010} mode of the manufactured cavity is 2.498 GHz and the measured (unloaded) Q is 8990 ± 5; higher Q could be obtained by using copper for the cavity walls, or by using silver internal coatings, but these benefits are minimal when compared with the reduced cost and ease of machining when using bulk aluminium metal.

Details regarding the TM_{010} cavity and its measurement of CMC samples are shown in Fig. 4, which is constructed from two mirror-image pieces that clip together to form a cylinder (Fig. 4a). No microwave surface currents flow across the joint formed between the two pieces in the TM_{010} mode; instead, the surface currents flow parallel to the faces of the joint, meaning that a sample gap of uniform width of a few mm can be opened between them without significantly compromising Q (it decreases at large gaps owing to increased radiation loss from the open slot thus formed).

All microwave measurements are taken with an Agilent E5071B vector network analyser (VNA) with computer control (Fig. 4b) at room temperature (nominally 20 °C); care should be taken in controlling the laboratory temperature to within a range of 2 °C as sample dielectric properties are temperature dependent (especially loss). Magnetic coupling to the TM_{010} mode is achieved using a pair of identical, loop terminated, flange-mounted SMA connectors, which are connected to the VNA by a pair of flexible coaxial cables. The loop is made of a silver-coated copper wire of 1 mm diameter soldered between the inner conductor and the extruded (4 mm long) outer conductor of the SMA connector. Due to the wall thickness of 8 mm, most of the loop is within the cavity wall and only a small portion of the tip of the loop protrudes into the cavity area. To make up for this and optimise the coupling strength, the coupling loops are placed diametrically opposite to each other, half-way up the curved wall of the cavity, and have their planes oriented parallel to the axis of the cavity for maximum flux linkage (i.e. maximum coupling) to the magnetic field of the TM_{010} mode. This configuration allows us coupling strength of about 20 dB of insertion loss, S_{21}, at resonance, as shown in Figs. 5–7. Two-port measurements of the resonant frequency, f, loaded quality factor Q_L, 3 dB bandwidth $f_B = f/Q$ and insertion loss L at resonance, are taken directly from the markers added to the VNA plot of the magnitude of voltage transmission coefficient S_{21} in the frequency domain. The combined cable losses are measured to be 0.74 ± 0.01 dB at 2.4 GHz. The unloaded Q is calculated from loaded (measured) quality factor Q_L by first measuring the insertion loss L (in dB) at resonance (with cable losses subtracted) and then using $Q = Q_L/(1-\beta)$, where $\beta = 10^{-L/20}$ [27]. This analysis assumes symmetric (i.e., identical) coupling at each microwave port, and is

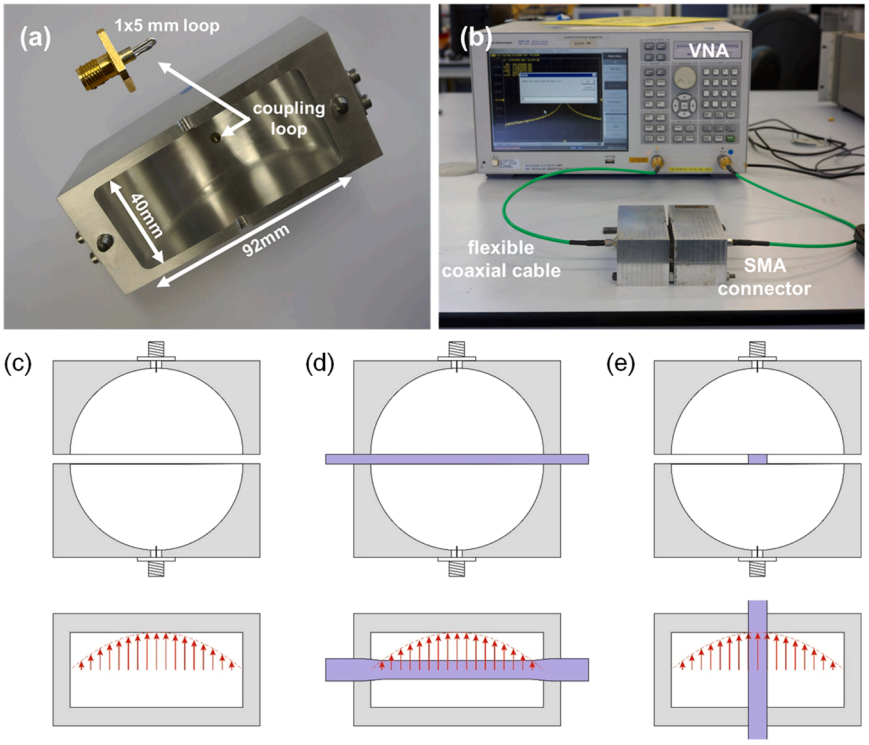

Fig. 4. (a) Image of one half of the cylindrical aluminium cavity; (b) the cavity connected to a VNA for sample measurement (here the cavity holds a PTFE rod used for calibration); (c) schematic diagram of the plane and side elevations of the empty cavity with a 5.1 mm gap opened up to accept a 5.0 mm thick CMC sample in both (d) perpendicular and (e) parallel sample orientations (with respect to the direction of the applied microwave E field, shown in red in (c)-(e)).

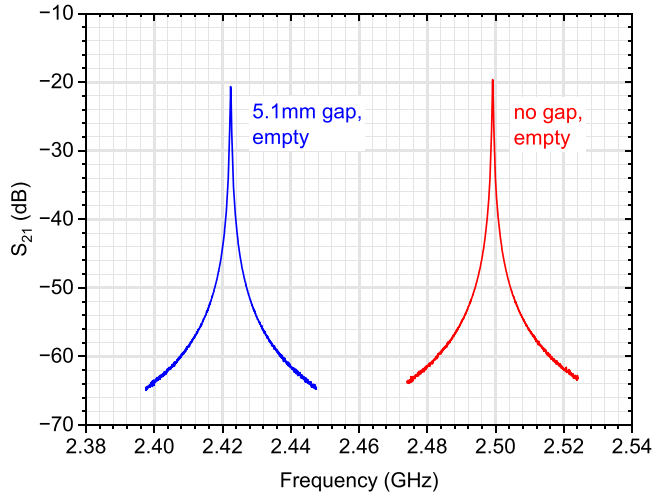

Fig. 5. The comparative performances of the TM_{010} cavity, via measurement of the voltage transmission coefficient S_{21} in the frequency domain, with no gap (red trace, $f = 2.498$ GHz, $Q = 8890 \pm 5$) and with a 5.1 mm gap (blue trace, $f = 2.422$ GHz, $Q = 8450 \pm 5$). The Q-factor is sufficiently large enough with the gap to allow cavity perturbation measurements to be easily performed on the CMC samples, slid in and out of the cavity in the orientations shown in Fig. 4(d) and (e).

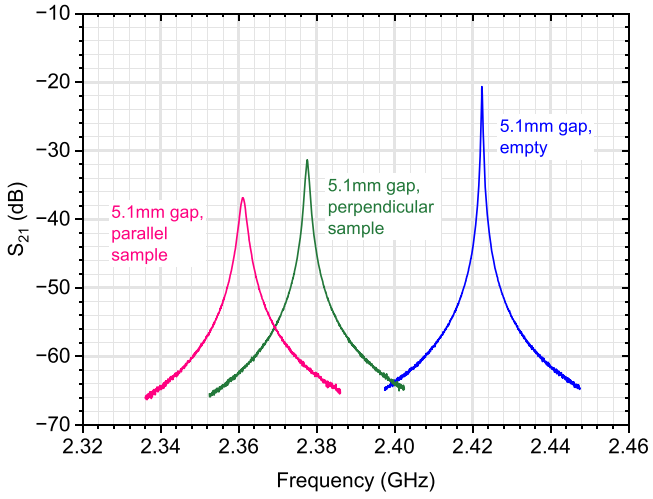

Fig. 6. Dielectric characterisation of a 3D printed, low-density PLA sample, of the same nominal shape and size as the standard CMC samples. As expected, the parallel sample has the largest induced electric dipole moment giving the greatest TM_{010} cavity perturbations, both for resonant frequency and Q-factor. Data in the parallel orientation give values for the complex permittivity of the 3D-printed PLA samples of $\varepsilon_1 = 1.92 \pm 0.05$ and $\varepsilon_2 = 0.024 \pm 0.001$.

established experimentally by adjusting the size of the coupling loops so that measured values of voltage reflection coefficients at resonance S_{11} and S_{22} are near equal. All Q factors quoted in this paper are unloaded values, but these differ little from Q_L for CMC measurements since the samples reduce Q to around 400 so that the coupling correction $b << 1$; in practice, the coupling correction only needs to be applied for Q measurements for the empty cavity.

The accommodate the standard CMC sample (and variations thereof) we allow for a 5.1 mm wide, fixed gap between the two cavity halves (Fig. 4c), allowing the 5.0 mm thick CMC sample to be easily inserted into (and removed from) either the "perpendicular" or "parallel" orientations shown in Fig. 4d and Fig. 4e, respectively; these directions are defined relative to the direction of the applied (axial) electric field E_0, which is shown in red in Fig. 4c-e. The comparative experimental performances of the TM_{010} cavity with and without a 5.1 mm gap are shown in Fig. 5 in the form of VNA measurements of the voltage transmission

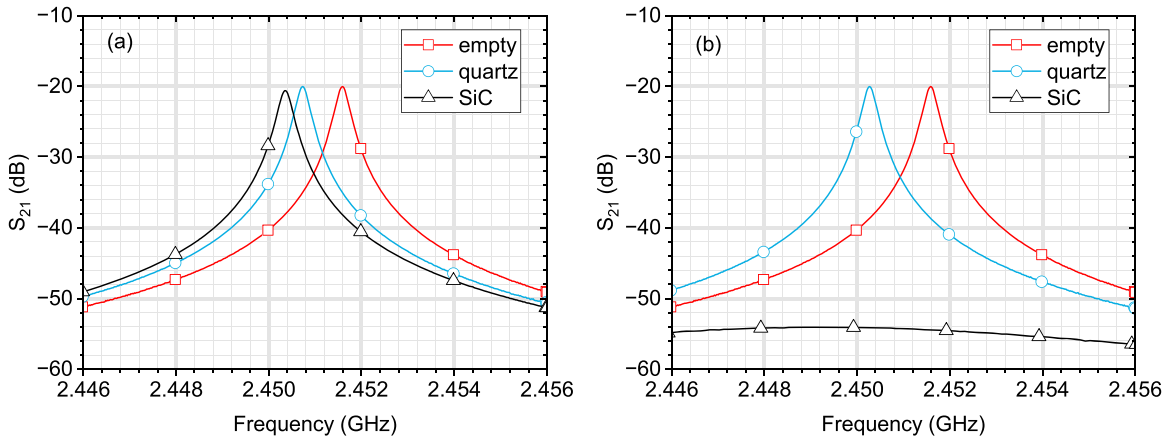

Fig. 7. Characterisation of × 500 bundle of 10 mm diameter SiC fibres contained within a fused quartz tube, with the microwave electric field oriented (a) perpendicular to the sample, and (b) parallel to the sample. In (b), the huge reduction in Q (from 8890 to 160) is a result of the high electrical conductivity of the fibres; in (a) the internal electric field is reduced to almost zero by depolarisation, so there is negligible reduction in Q to within experimental error.

coefficient S_{21}; introducing the gap in an empty cavity reduces the TM_{010} resonant frequency from 2.498 GHz to 2.422 GHz, and Q from 8990 ± 5 to 8450 ± 5. These values for the split cavity are highly stable (to 0.001 % for f and 0.05 % for Q) and so enable the use of this split configuration for highly sensitive dielectric characterisation of the SiC_f/SiC CMC samples via cavity perturbation, with each measurement taking approximately two seconds to perform (i.e. limited by the time taken to insert or remove the sample).

2.3. Cavity perturbation method

Energy losses in the cavity are quantified using $1/Q$, for which we can also use the 3 dB bandwidth $f_B = f/Q$. Note that from the four experimental parameters associated with the cavity resonance f, f_B, Q_L and L, one (f) is linked to energy stored whilst the other three (f_B, Q_L and L) are highly correlated and are linked to energy loss. When a sample is measured using the cavity perturbation method, these are related to sample polarisation and loss, respectively, so we get two "pieces" of dielectric information in each sample measurement. The sample's interaction with the cavity's applied electric field E_0 (assumed uniform here but this need not be the case) is quantified via its induced electric dipole moment p. This can be measured experimentally from the changes in resonant frequency Δf and microwave losses $\Delta(1/Q)$ on inserting the sample, using a modified form of first order cavity perturbation theory [28,29], as given in Eqs. (1) and (2):

$$\frac{\Delta f}{f_0} \equiv \frac{f_s - f_0}{f_0} \approx \frac{-\mathrm{Re}(pE_0)}{4U_e} \propto -Re(p) \tag{1}$$

$$\Delta\left(\frac{1}{Q}\right) \equiv \frac{1}{Q_s} - \frac{1}{Q_0} \approx \frac{-Im(pE_0)}{2U_e} \propto -Im(p) \tag{2}$$

where the subscript "s" refers to the cavity with the sample present and "0" to the empty cavity; U_e is the total stored energy in the electric field and E_0 is the applied electric field magnitude for the empty cavity. The greatest cavity perturbation (and so the most sensitive dielectric measurement) is when the maximum p is induced for a given E_0. This occurs when field depolarisation effects are minimised, i.e., for long samples placed along the cavity axis, when the electric field boundary condition ensures a large electric field within the sample; however, this is not the ideal sample orientation for standard CMC, owing to the large microwave absorption (and hence loss) associated with the highly conducting SiC fibre tows that run the length of the samples and so reduce Q to a value that is too small to measure (we will revisit this point below).

To illustrate the effects of sample orientation on cavity measurement, a PLA sample of the same shape and nominal dimensions as for the standard CMC samples was used in the finite element simulation and measurement. PLA was selected due to its well-known dielectric properties and the ease with which it can be obtained through 3D printing and modelled in finite element simulation. Fig. 6 shows measurements of a 3D-printed PLA sample. There is a higher induced electric dipole moment p in the parallel orientation, where the samples internal electric field E_1 is large and approximately equal to the applied field E_0 (since there is little field depolarisation except near the sample ends) and this produces the largest cavity perturbations for both f and Q. In the perpendicular orientation there is significant reduction in E_1 compared with the applied field E_0 owing to the high density of polarisation charges that are induced on the flat sample surface perpendicular to the E-field; hence p is reduced and so too are the cavity perturbations. For the empty cavity, $f_0 = 2.422$ GHz and $Q_0 = 8450 \pm 5$, whilst for the PLA sample in the perpendicular orientation $f_s = 2.377$ GHz and $Q_s = 2410 \pm 4$, and in the parallel orientation $f_s = 2.361$ GHz and $Q_s = 1330 \pm 3$.

The cavity measurements in the parallel orientation can be used with Eqs. (1) and (2) to calculate the complex (relative) permittivity of the PLA sample. If we assume that there is no E-field depolarisation in the parallel geometry then $p \approx (\varepsilon - 1)\varepsilon_0 E_0 V_s$, where $\varepsilon_0 = 8.85 \times 10^{-12}$ F/m is the permittivity of free space and V_s is the PLA sample volume within the E-field. Eqs. (1) and (2) can now be used explicitly to calculate real and imaginary parts of the complex permittivity $\varepsilon = \varepsilon_1 - j\varepsilon_2$ by writing:

$$\varepsilon_1 \approx 1 + \frac{2V_m}{V_s}\frac{\Delta f}{f_0}, \tag{3}$$

$$\varepsilon_2 \approx \frac{V_m}{V_s}\Delta\left(\frac{1}{Q}\right) \tag{4}$$

where V_m is defined to be the effective volume occupied by the electric field energy (also known as "mode volume"); this is approximately 27.0 % of the internal cylindrical volume of the TM_{010} cavity, which is itself increased by approximately 7 % owing to the 5.1 mm gap, so that $V_m = 76.7 \pm 0.3$ cm^3 based on a standard error of 0.05 mm in each cavity dimension. Taking the PLA sample to have $V_s = 2.00 \pm 0.05$ cm^3 gives $\varepsilon_1 = 1.92 \pm 0.05$ and $\varepsilon_2 = 0.024 \pm 0.001$; these values are underestimates of the PLA permittivity since the 3D printed sample is less than 100 % dense; this agrees with published values of 3D printed PLA, for which the static value of ε_1 is in the range 1.78 to 2.81, depending on the density [30].

2.4. Measurement of SiC fibres

To further understand the microwave E-field interaction with standard CMC samples and to deal with the inherent electrical anisotropy

associated with the highly conducting SiC fibres (~10 mm diameter), we measured a bundle of around 500 SiC fibres, which would typically form a single tow in the CMC material. The tow was cut to a length of 10 cm and threaded into a cylindrical, fused quartz tube (of inner and outer diameters of 1.5 mm and 1.8 mm, respectively, and length 10 cm; CM Scientific Ltd., Silsden, UK). The tube has a very low microwave loss and is used as a carrier to orient the SiC fibre tows in the parallel and perpendicular orientations of the TM_{010} cavity mode.

Measurements of S_{21} for the SiC fibre tow are shown in Fig. 7. The extreme anisotropy in microwave loss (observed in the large reduction of Q in the parallel orientation) is an extreme form of the behavior exhibited by the PLA samples and is easily explained by consideration of the size of the electric field E_1 that results inside each of the SiC fibres. The frequency shift Δf is associated with the total induced dipole moment p and the change in microwave loss $\Delta(1/Q)$ (or Δf_B) is associated with the quantity $\sigma \cdot E_1^2$, which is the power absorbed (and hence dissipated) per unit volume, where s is the electric conductivity of the fibres. In the perpendicular orientation Fig. 7a, E_1 is reduced greatly compared to the applied electric field E_0 owing to the high density of polarisation charges induced on the cylindrical surfaces of each fibre; the associated induced dipole moment gives a reduced resonant frequency but the (almost) complete extinction of E_1 means that there is little microwave loss (even though s remains high), so there is negligible reduction in Q compared with that of the cavity and empty sample tube. In contrast, in the parallel orientation (Fig. 7b), the continuity of parallel electric field means that E_1 is approximately the same as E_0 and the loss term $\sigma \cdot E_1^2$ is comparatively very large, so that there is a large reduction in Q (from 8990 ± 5 to 160 ± 5); note that the sample polarisation is similar to the perpendicular orientation, so there is a comparable (small) frequency shift Δf.

We can extrapolate this result to the measurement of a standard CMC sample, noting that while the volume fraction of fibres in the cavity is larger for the perpendicular than the parallel orientation (Fig. 4), due to the woven structure of the CMC, their interaction with the microwave E field are significantly different. When the fibres predominantly align with the axis of the cavity (as in the parallel CMC sample orientation) they are so conductive that they make the TM_{010} mode impossible owing to the E-field boundary condition at their surfaces, and instead a higher order coaxial mode is excited at a much higher frequency. Although, with the CMC sample in the perpendicular orientation there are fibres aligned along the same axis, because they only extend over a short portion of axis they are not capable of altering the TM_{010} mode in the same way. The lower limit for reliable Q measurement is about 50, so it only takes three or four fibre tows across the length of the cavity in the parallel orientation to effectively extinguish the TM_{010} resonance. Hence, we can only characterise standard CMC samples in the perpendicular geometry, but this raises an important point. Of crucial importance to the assessment of damage in CMC samples that follows is that in the parallel geometry the microwave response is dominated by the electrical conductivity of the SiC fibres, but in the perpendicular geometry it is less sensitive to the fibres (within which the E-field is effectively zero), and instead sensitive to the regions between the fibres (i.e., SiC matrix and BN interphase) where the E-field is now concentrated; which are the regions which are more susceptible to environmental degradation.

2.5. Calculation of the electrical conductivity of SiC fibres

To validate the cavity perturbation method to characterise SiC fibres we use measurements in the parallel orientation to estimate the electric conductivity s of the fibres in a totally contactless way and compare it with known values. We use the same analysis as used for the complex permittivity calculation of the PLA sample of Section 2.3. The "active" part of the sample within the cavity has length of 40.00 ± 0.05 mm, so that the total fibre volume V_s is calculated from their number (500) and diameter (10.0 ± 0.1 μm). Experimentally it is found that $\Delta(1/Q) = 0.0064 \pm 0.0001$ between the empty and fibre-loaded quartz tubes, so that $\varepsilon_2 = 295 \pm 9$, quoting standard errors based on three independent measurements of three fibre tows. For a good electrical conductor such as SiC, electrical conductivity is related to the loss term ε_2 by $\sigma = 2\pi \cdot f \cdot \varepsilon_0 \cdot \varepsilon_2$, resulting in $\sigma = 41 \pm 2$ S/m at 2.45 GHz.

To check this value over a range of microwave frequencies, '40 fibres were separated from a full tow and measured (again using the quartz sample tube) along the axis of a second (gapless) cylindrical resonator of inner radius 46 mm and inner length 36 mm, used for standard dielectric property measurement of samples. This cavity was operated in its TM_{010}, TM_{011} and TM_{012} modes at 2.49 GHz, 4.84 GHz and 7.07 GHz, respectively, yielding values of ε_2 of 297 ± 10, 164 ± 6 and 112 ± 4, corresponding to conductivities σ of 41 ± 2 S/m, 44 ± 2 S/m and 44 ± 2 S/m, respectively; averages and standard errors are based on three independent measurements of three different × 40 fibre bundles in three different sample tubes. Hence, we have four independent measurements yielding a constant SiC fibre conductivity (within experimental error) of 43 ± 1 S/m. This value agrees well with published DC conductivity data from conventional electrode-based measurements [31,32] and imply a simple Drude-type conductivity within the SiC fibres which is independent of frequency.

2.6. Finite element modelling (COMSOL) of cavity perturbation

We use COMSOL Multiphysics for finite element modelling where no analytic solutions exist, namely to model (a) the EM field distribution in the cavity with the sample slot, and (b) the polarisation and loss of the typical CMC sample geometry, of rectangular cross section, where the microwave E-field is applied perpendicular to the long direction of the sample; this is primarily to allow the extraction of absolute values of complex permittivity from the microwave cavity data.

The full 3D model of a slotted cavity (with 5.1 mm wide slot), its microwave ports (two coupling loops) and the CMC-type sample is shown in Fig. 8. Even with the slot, the normalised E-field distribution of the TM_{010} mode around the sample in Fig. 8b differs little from the theoretical field plot of Fig. 8d for the ideal cylinder. The model was validated by comparing the COMSOL cavity parameters when loaded with a PLA sample with the experimental PLA results, with the comparison summarised in Fig. 8c and d The PLA sample in the COMSOL model represents an effective dielectric material, which is a common method of extracting dielectric properties of unknown sample of complex geometry. The COMSOL and experimental values agreed well for the resonant frequencies and Q factors for the four scenarios of empty cavity with no gap, empty cavity with gap, perpendicular PLA sample in a cavity with gap and parallel PLA sample in a cavity. This gave us confidence in using the cavity with the 5.1 mm gap to measure samples of the standard CMC geometry.

Dielectric properties for standard CMC samples in the perpendicular orientation must be extracted by finite element modelling since no analytic formulae apply for this complex geometry, of rectangular cross-section. Polarisation charges develop on the flat surfaces perpendicular to the microwave E-field and these reduce the field E within the sample (with a greater reduction for higher values of ε_1), thus causing the polarisation to limit to a finite value as ε_1 increases (as it would for a metal), also causing a reduction in loss for a fixed value of ε_2 since loss is proportional to $\varepsilon_2 \cdot E_1^2$. Calibration curves for extraction of absolute values of complex permittivity from sample measurements of polarisation $-\Delta f/f_0$ (defined in Eq. (1)) and loss $\Delta(1/Q)$ (defined in Eq. (2)) are shown in Figs. 9a and 9b, respectively. CMC samples studied here have complex permittivity values in the low loss limit $\varepsilon_2 << \varepsilon_1$, within which the polarisation is a universal function of ε_1 and is approximately independent of ε_2 (Fig. 9a). The reduction of internal E-field with increasing ε_1 is evident in the saturation seen in Fig. 9a; this is also associated with the decreased loss in Fig. 9b as ε_1 increases for a fixed value of ε_2. Another useful approximation in the low loss limit (evident in Fig. 9b) is that is proportional to ε_2, with the scaling constant

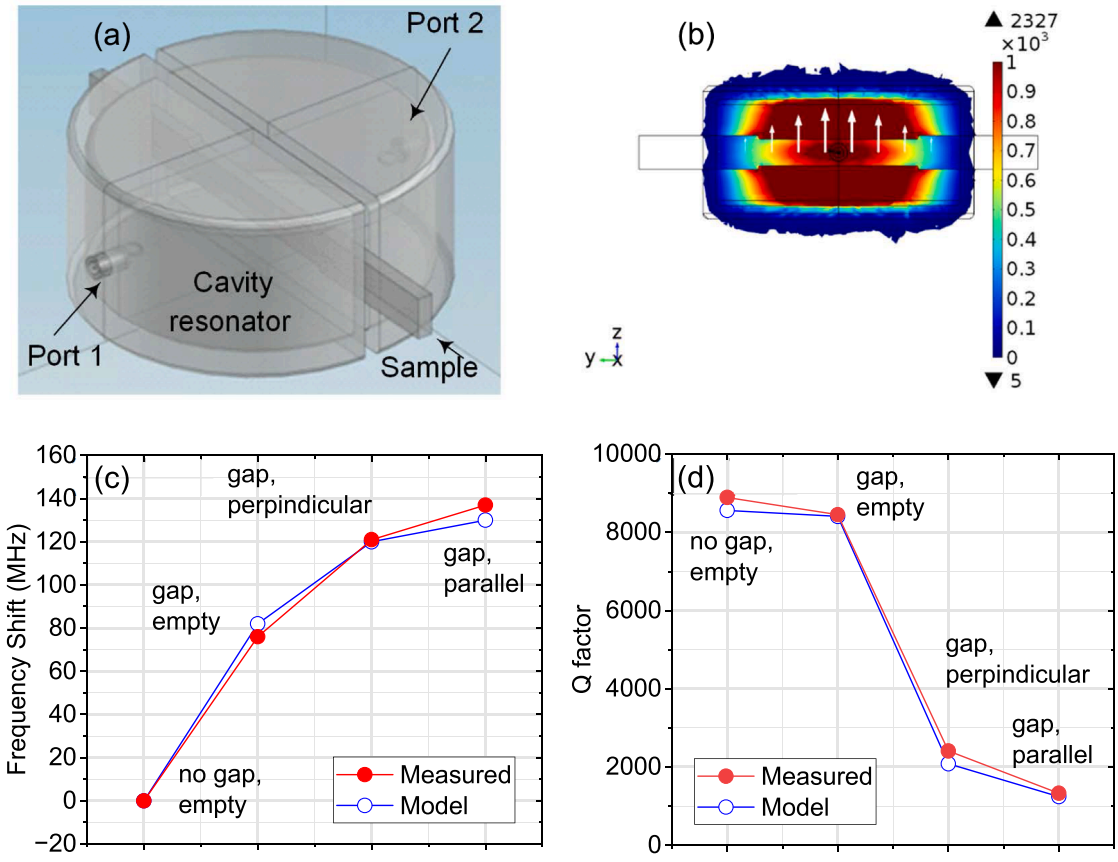

Fig. 8. Finite element modelling and validation. (a) 3D geometry of the resonant cavity and CMC-type sample. (b) Cross-sectional normalised electric field distribution around the sample. Arrow indicates the electric field vector. Comparison of trends in (c) frequency shift and (d) Q factor between simulation and measurement according to the conditions described in Figs. 4 and 5.

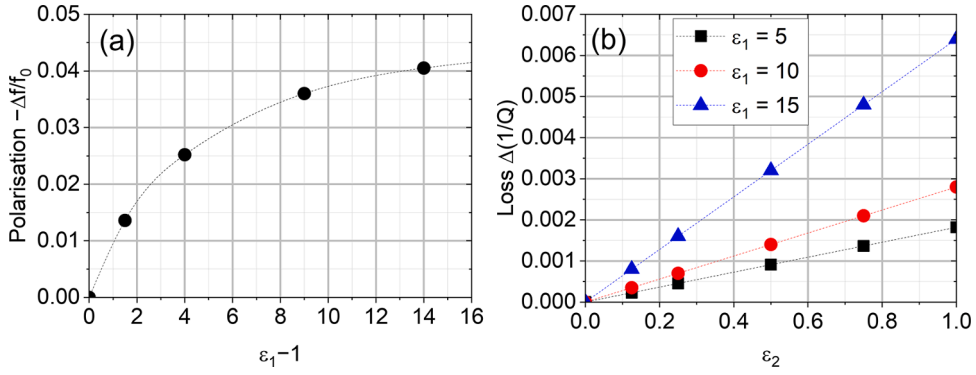

Fig. 9. Calibration curves of perpendicular samples produced by parametric sweeps in COMSOL Multiphysics. (a) Polarisation as a function of $\varepsilon_1 - 1$, a universal curve on the assumption that $\varepsilon_1 >> \varepsilon_2$, as for the CMC samples here. (b) Loss as a (linear) function of ε2 for three different values of ε_1 (black = 5, red = 10, blue = 15).

depending on ε_1.

Calculation of the complex permittivity of any sample of the CMC geometry is now straightforward; firstly, using the universal calibration curve of Fig. 9a to calculate ε_1 from the experimental value of sample polarisation; secondly, this value of ε_1 is used with the experimental value of sample loss and the calibration curves of Fig. 9b to calculate ε_2.

2.7. Environmental exposure conditions

To assess the potential of using the cavity perturbation method to detect environmental degradation in SiC_f/SiC CMCs, it was important to determine the repeatability of measurements for a single sample, as well as within a small acceptable population. As a result, sample polarisation $-\Delta f/f_0$ and loss $\Delta(1/Q)$ (as per Eqs. (1) and (2), relating to sample polarisation and sample loss, respectively) were measured for six as-received CMC samples, with average values and standard errors calculated from six repeated measurements of each; results for this initial set are presented in Section 3.2.

Once a suitable level of confidence was established, similar measurements of $-\Delta f/f_0$ and $\Delta(1/Q)$ were repeated for a further nine as-received CMC samples. After the initial measurements, each of the samples was exposed to one of three environmental exposure conditions

and measured again post-exposure. The details of each pre-exposure (PE) condition used are listed in Table 1. Three of the samples were exposed to PE1, which consisted of heating the samples to 800 °C and holding for 500 h in an air furnace (SNOL, Lithuania), three were exposed to PE2, which involved exposing the samples to 95 % relative humidity at 65 °C for 500 h using a climate humidity chamber (Binder Dynamic, Germany) followed by an short at 800 °C (20 min), and three were exposed to PE3, which consisted of the same humidity conditions as PE2, however with a significantly shorter period at 800 °C (20 min).

The three pre-exposure conditions were selected based on previous research conducted by Diaz et al. [21], who confirmed that low temperature water exposure at 65 °C caused degradation of the BN interphase layer, opening free paths for oxygen ingress and embrittlement upon reheat. The result was a degradation in the macroscopic mechanical properties of SiC_f/SiC CMC samples exposed to such conditions.

The three different types of pre-exposed CMC samples are shown in Fig. 10. There is a clear visual difference between each sample after their respective environmental exposure. PE3 appears to have the most severe discolouration, seen as a blackening of the sample, closely followed by PE1, whereas PE2 only has a mild discolouration seen in the form of a blue tint, most noticeable within the gauge section of the sample.

2.8. Microstructural and mechanical characterisation

Microstructural, mechanical and fractographic analyses were conducted on CMC samples exposed to each type of pre-exposure condition, as well as on an as-received sample for comparison. Microstructural analysis was performed using a Zeiss Axio Observer Microscope at × 1000 magnification. Images were captured from polished side sections that had been cut and mounted in Bakelite prior to investigation. Mechanical characterisation was carried out by means of monotonic tensile testing. Tensile tests were performed using an Instron servo-hydraulic test frame (Instron, USA), in position control using a displacement rate of 0.1 mm/min, with strain monitored using a 12.5 mm extensometer. An example of the tensile test setup can be seen in Fig. 11. Finally, fractography was conducted using a Hitachi SU3500 (Hitachi, Japan) scanning electron microscope (SEM) under back scatter electrons (BSE).

3. Experimental results on CMC samples

3.1. The split TM_{010} cavity and preferred CMC sample orientation

For all CMC samples we repeat the measurements with the split TM_{010} cavity as for the PLA samples described in Section 2.3., noting the two sample orientations shown schematically in Fig. 4d-e. The orientational anisotropy of microwave loss has major implications for use of microwaves in assessment of CMCs. The three orientations of the CMC samples relative to the applied microwave *E*-field are shown in Fig. 12; in (a) there is huge microwave loss owing the large volume fraction of SiC fibres aligned parallel to the *E*-field, leading to the TM_{010} mode being extinguished; in (b) there is a much smaller volume fraction of SiC fibres aligned along the *E*-field and *Q* for the TM_{010} mode remains measurable (in the range 350 – 500 for as-received samples), with an acceptable 5.1 mm gap in the cavity; in (c), there is a very small volume fraction of SiC along the *E*-field, but the 9.5 mm width of the gauge section requires a 10 mm cavity gap, which is too large *since* radiation losses from the gap reduces the *Q* of the empty cavity. For these reasons,

Table 1
Environmental exposure conditions.

Sample ID	Humidity	Heat Treatment
PE1–1	n/a	500 h at 800 °C
PE1–2	n/a	500 h at 800 °C
PE1–3	n/a	500 h at 800 °C
PE2–1	500 h at 95 % humidity 65 °C	20 min at 800 °C
PE2–2	500 h at 95 % humidity 65 °C	20 min at 800 °C
PE2–3	500 h at 95 % humidity 65 °C	20 min at 800 °C
PE3–1	500 h at 95 % humidity 65 °C	500 h at 800 °C
PE3–2	500 h at 95 % humidity 65 °C	500 h at 800 °C
PE3–3	500 h at 95 % humidity 65 °C	500 h at 800 °C

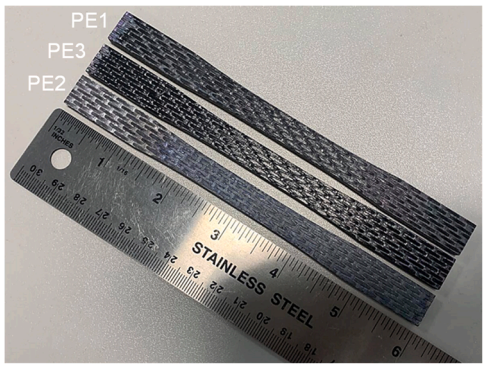

Fig. 10. Pre-exposed CMC samples; PE1, PE2 and PE3.

Fig. 11. Tensile test setup using 12.5 mm gauge extensometer.

Fig. 12. The three sample orientations relative to the microwave E-field in the TM_{010} cavity, showing the main orientation of the SiC fibre tows that run the full length of the CMC samples. All measurements of environmental damage are in (b), the perpendicular sample orientation, with a 5.1 mm cavity gap to allow the sample to be inserted and removed easily.

(b) is a good compromise and is the orientation used for all CMC sample measurements. Since there is no contribution to the microwave loss $1/Q$ arising from fibres oriented perpendicular to the microwave E-field (see Fig. 7a), sample loss is now sensitive to the bulk CMC sample, (not only the fibre tows) and hence is also sensitive to environmental degradation, which we seek to assess using the cavity perturbation method.

3.2. Variability in microwave dielectric properties of as-received CMC samples

The results of the repeatability trial are listed in Table 2, where the fractional frequency shifts (i.e., sample polarisation, as per Eq. (1)) and changes in reciprocal Q-factors (i.e., sample loss, as per Eq. (2)) are displayed for the first set of six as-received CMC samples. The average values and standard errors shown in Table 2 are from six independent measurements of each sample, for which the standard errors are very small (typically ±0.02 % in polarisation and ±0.1 % in loss). Such measurement errors are ignored after this point in the paper since what is more relevant is the average value and standard error for the set of six, or sub-sets of three for the exposure studies. This set of six's average value and standard error are for the polarisation $-\Delta f/f_0 = 0.02191 \pm 0.00005$ and for the loss $\Delta(1/Q) = 0.00202 \pm 0.00003$.

From the data of the first set of six samples we note that the sample losses are uncorrelated with the sample polarisation, with the fractional standard error for loss being an order of magnitude larger than the fractional standard error for polarisation. This implies that the variability from sample to sample is not due to sample dimensions (i.e., sample volume, since then both polarisation and loss should be proportional to volume and so highly correlated) but more likely due to variability in their microstructures. The individual results for all six samples sit comfortably within three standard deviations either side of their mean values, which gave us high confidence in proceeding with investigating the effects of systematic damage using a second set of nine samples, split into sets of three for different environmental exposure conditions.

Also shown in Table 2 (for completeness) are the values of complex permittivity ε_1 and ε_2 for each of the original samples, calculated from the cavity perturbation measurements with the aid of the COMSOL modelling of Section 2.6 (Fig. 9). Since the real permittivity ε_1 changes only by a small amount from sample to sample, to a very good approximation we can consider the experimental values of $-\Delta f/f_0$ and $\Delta(1/Q)$ to be proportional to $\varepsilon_1 - 1$ and ε_2, respectively, so for the rest of this paper we use changes in these experimental parameters to quantity the changes in the dielectric properties of the samples.

Table 2
Sample polarisation $-\Delta f/f_0$ and sample loss $\Delta(1/Q)$ relative for the first set of six as-received CMC samples, measured in the split TM_{010} cavity at 2.422 GHz, with (small) standard errors calculated from six independent measurements of each sample. Also shown are the complex permittivity $\varepsilon = \varepsilon_1 - j\varepsilon_2$ calculated for these samples (precise to three significant figures) using the COMSOL modelling described in Section 2.6.

Sample Number	Sample Polarisation $-\Delta f/f_0$	Sample Loss $\Delta(1/Q)$	e_1	e_2
1	0.021858 ± 0.000004	0.002161 ± 0.000002	3.96	0.210
2	0.021911 ± 0.000003	0.002075 ± 0.000002	3.97	0.202
3	0.021898 ± 0.000003	0.002012 ± 0.000002	3.97	0.196
4	0.021724 ± 0.000002	0.001962 ± 0.000001	3.93	0.191
5	0.021988 ± 0.000003	0.001959 ± 0.000003	3.99	0.191
6	0.022083 ± 0.000005	0.001974 ± 0.000002	4.01	0.192

3.3. Environmental exposure results

Fig. 13 is a plot of S_{21} of the microwave cavity when empty and loaded with a CMC sample, here having undergone pre- and post-environmental exposure. Fig. 14 shows the microwave cavity results collected for the full, second set of nine as-received CMC samples, split into 3 sets of 3 for each type of environmental exposure listed in Table 1 (PE1–3). Whilst there are clear changes in loss across the samples in Fig. 14b between pre- and post-exposure, there appears to be little change in polarisation in Fig. 14a; however, by plotting the % changes between pre- and post- exposure for both polarisation (Fig. 14c) and loss (Fig. 14d) the three sets of samples become clearly differentiated by their exposure conditions, summarised quantitatively in Table 3. Samples exposed to PE1 and PE3 experienced a significant increase in loss (of +27.8 % and +21.5 %, respectively), with an order of magnitude less for PE2 (+2.2 %). This trend is reflected in the increases in polarisation, with PE3 having the greatest change (+2.9 %) but of similar magnitude to PE1 (+2.4 %), the order reversed compared to loss, with PE2 changes (+0.25 %) being an order of magnitude less.

3.4. Effect of exposure on microstructures

Fig. 15 displays the micrographs for one of the as-received CMC samples and following each of the three pre-exposure conditions PE1–3, with the polished sections taken ~1 mm from the edge of the CMC. These reveal some subtle variations between the microstructures, specifically regarding the BN interphase layer in comparison to the as-received microstructure (Fig. 15a). The PE1 (Fig. 15b) sample, which was heated to 800 °C and held for 500 h, shows no significant signs of degradation, with the interphase layer remaining largely intact, although a level of oxidation is expected. The PE2 (Fig. 15c) sample on the other hand, which was held at 20 min at 800 °C following 500 h at 95 % humidity 65 °C exposure, shows severe signs of degradation of the BN interphase, which has changed in thickness and morphology; previous research has shown that Si, B and N are co-localised under such conditions [21]. Lastly, the PE3 (Fig. 15d) sample, which was held for 500 h at 800 °C following the humidity exposure, shows that the majority of the BN interphase has been removed due to volatilisation over a longer period of time, this leaving a gap between the fibres and matrix.

3.5. Effects of exposure on tensile testing

Fig. 16 displays tensile testing results for the four different types of CMC samples, the as-received (AR) sample used as a baseline comparison, together with samples that had been subject to the three exposure conditions PE1-PE3; the corresponding ultimate tensile strength (UTS) and strain to failure data are presented in Table 4.

The AR CMC sample exhibits the best mechanical properties when compared to the other pre-exposed CMC samples. PE1 shows similar results to the AR sample, with a small reduction in UTS with the same strain to failure. PE3 exhibits the worst desirable mechanical properties of all four CMC samples, with low UTS and strain-to-failure being indicative of a brittle failure, alluding to loss of the BN interphase and ultimate loss of the fundamental CMC strengthening mechanism. The stress-strain response for PE2 takes on a different form to the other tensile curves, appearing serrated in the "plastic" region of the curve beyond the proportional limit, showing some level of ductility, along with a greatly decreased UTS. This response is attributed to the partial degradation and removal of the BN interphase, which leads to a mixed mode of damage accumulation during mechanical loading.

3.6. Fractography

Fig. 17 displays the fracture surfaces for the AR and PE1–3 CMC samples. The images were captured at a section on the edge of each fracture surface using BSE-3D imaging. Upon inspection, there are clear

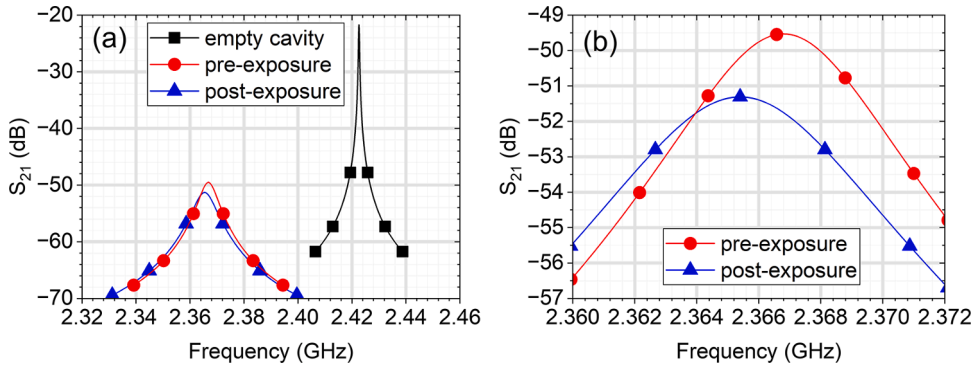

Fig. 13. Dielectric characterisation of a CMC sample before and after environmental exposure, in this case sample PE1–1 from Table 1 (a) The empty cavity (black), loaded with the pre-exposed sample (red), then loaded with the post-exposed sample (blue). (b) Expanded plot, showing the differences between the pre-exposed (red) and post-exposed (blue) samples, the latter showing an increased polarisation and an even greater increased loss (in this case by +2.9 % and +25.6 %, respectively).

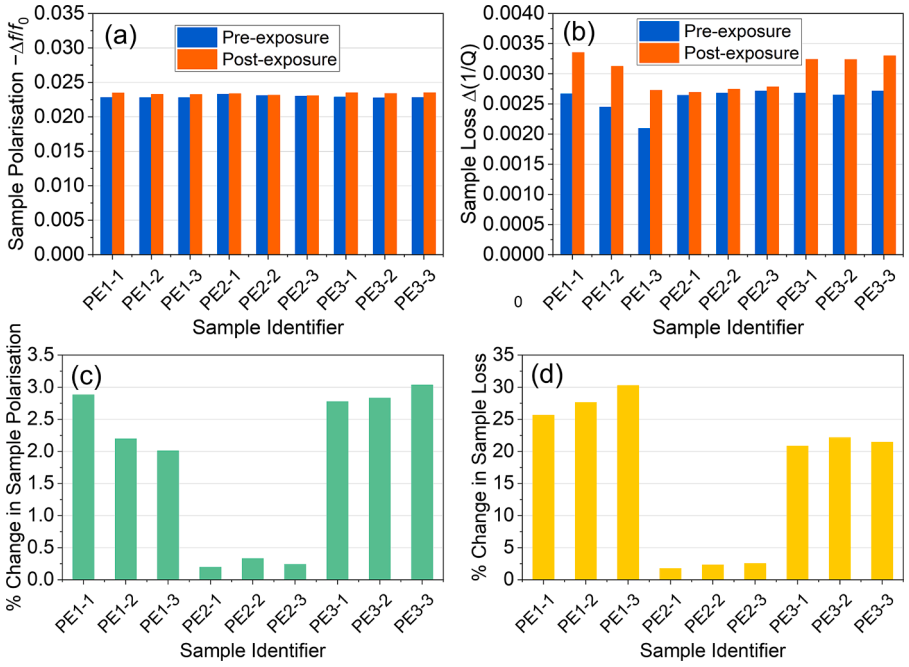

Fig. 14. (a) Sample polarisation and (b) loss for the second set of nine CMC samples before and environmental exposures. To emphasise the effects of each exposure PE1, PE2 and PE3, also plotted are (c) the % change in polarisation and (d) the % change in loss after exposure.

Table 3
The % increases in polarisation and loss for the three sets of three samples exposed to exposure conditions PE1-PE3; average values and standard errors are quoted for the three replicate samples within each exposure group.

Exposure	% Increase in Polarisation	% Increase in Loss
PE1	2.4 ± 0.3	27.8 ± 1.3
PE2	0.25 ± 0.04	2.2 ± 0.2
PE3	2.9 ± 0.1	21.5 ± 0.4

differences between each of the fracture surfaces. The AR sample exhibits significant levels of fibre pull-out, as desired; PE1 displays a slightly reduced level of fibre pull-out owing to the small level of oxidation of the BN interphase; PE2 has some evidence of fibre pull-out, although it also shows significant regions of brittle-type fracture, due to the changes previously indicated in the BN interphase; however, PE3 displays a wholly brittle fracture due to the removal of the BN interphase, supporting the tensile results presented in Fig. 16.

4. Discussion

The changes in mechanical and microwave cavity responses along with a description of the observed microstructural changes due to the environmental exposures relative to the as-received CMC are summarised in Table 5.

For PE1, which is held at 800 °C for 500 h, it is observed that the BN interphase layer remains largely intact when observing the microstructure. This is due to the formation of a silica-rich oxide that "wets" the entire surface of the material within the first couple of hours of exposure at 800 °C [33]. The surface SiC oxidises preferentially leaving behind an oxide scale that protects the underlying CMC from oxidative attack by expanding and closing off internal gas paths to the material below [34]. This slows down oxidation by forcing the oxygen to diffuse through a solid oxide layer, rather than having a direct path to the fibres and interphase layer [15]. The presence of a sufficiently thick, low permeability oxide layer results in the retention of the CMCs' mechanical properties within the bulk of the material. The fracture surface shows slightly less fibre pull-out than for the AR sample; however, the primary

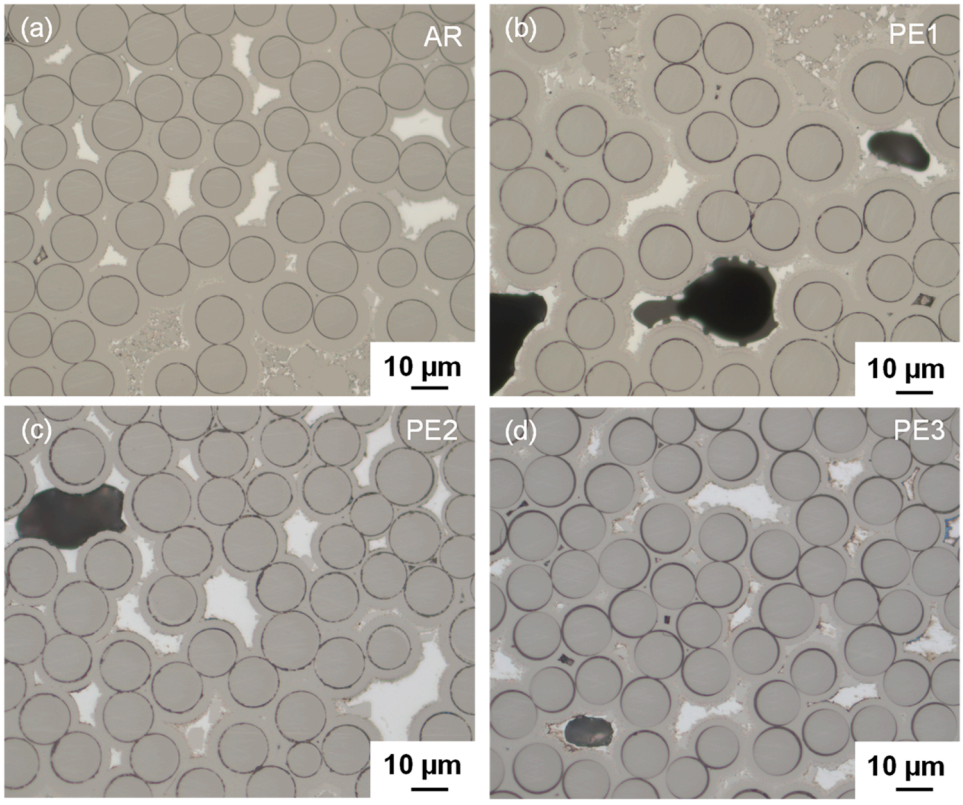

Fig. 15. Microstructure of the SiC_f/SiC CMC for the (a) as-received (AR) material and for the different exposure conditions (b) PE1, (c) PE2 and (d) PE3.

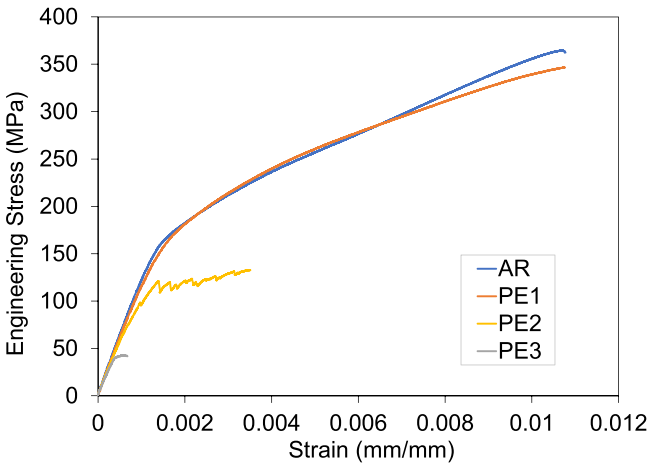

Fig. 16. Engineering stress-strain response for the as-received (AR) and post-exposed SiC_f/SiC CMC material (PE1–3).

Table 4
Ultimate tensile strength (UTS) and strain to failure data.

	UTS (MPa)	Strain to Failure (%)
As-received	364	1.08
PE1	345	1.08
PE2	133	0.35
PE3	43	0.07

toughening mechanism remains intact. It is worth noting that the silica scale is not present in the presented microstructure due to the grinding and polishing process. While there is little difference in mechanical properties compared with the AR sample, the microwave properties (both polarisation and loss) show pronounced increases. The increase in dielectric loss is the highest of the three PE sets (at +28 %) and is attributed to the amorphous silica layer [35–37] formed due to the high temperature exposure; it is well known that amorphous silica has a higher microwave loss than crystalline quartz.

For PE2, the addition of water vapour in the gas mixture results in a more rapid oxidation and depletion of the BN interphase layer (Fig. 15d). This is partially down to the absence of a protective SiO_2 scale, and partially down to the increased permeation of H_2O in the non-wetting oxides that form [33]. The BN interphase layer degrades as a result of the low temperature humidity exposure at 65 °C, leaving gaps between the matrix and the fibres. These annular voids leave the fibres unprotected, resulting in their oxidation and embrittlement in subsequent reheating regimes [21]. The microstructure for PE2 shows a significant degradation of the BN interphase layer; however, due to the short reheat period it is not yet fully depleted. The fracture surface shows some regions at the center of the sample where the fibres have fully oxidised and fused together, resulting in regions of severe embrittlement and regions towards the edge of the sample where the BN interphase is clearly absent. However, the fibres are unfused, which causes substantial fibre pull-out at lower stresses, due to the fibres and the matrix working independently. The microwave properties of PE2 show a small increase compared to the AR CMC sample (+2.2 % in dielectric loss, +0.25 % in polarisation). This is the case as the level of overall oxidation and formation of amorphous silica is minimal due to the short time at 800 °C (20 min), and the degradation of the BN interphase has little influence on the microwave properties.

The BN interphase layer appears to have been completely volatilised in PE3, which is supported by the large network of annular voids formed between the fibres and the CVI matrix within the microstructure. In its absence and subsequent extended reheat, SiC fibres have become fused to one-another, which results in a correlated fracture of embrittled fibres at significantly lower stresses [38], evidenced by the stress-strain response exhibiting very little strength and plasticity. For the

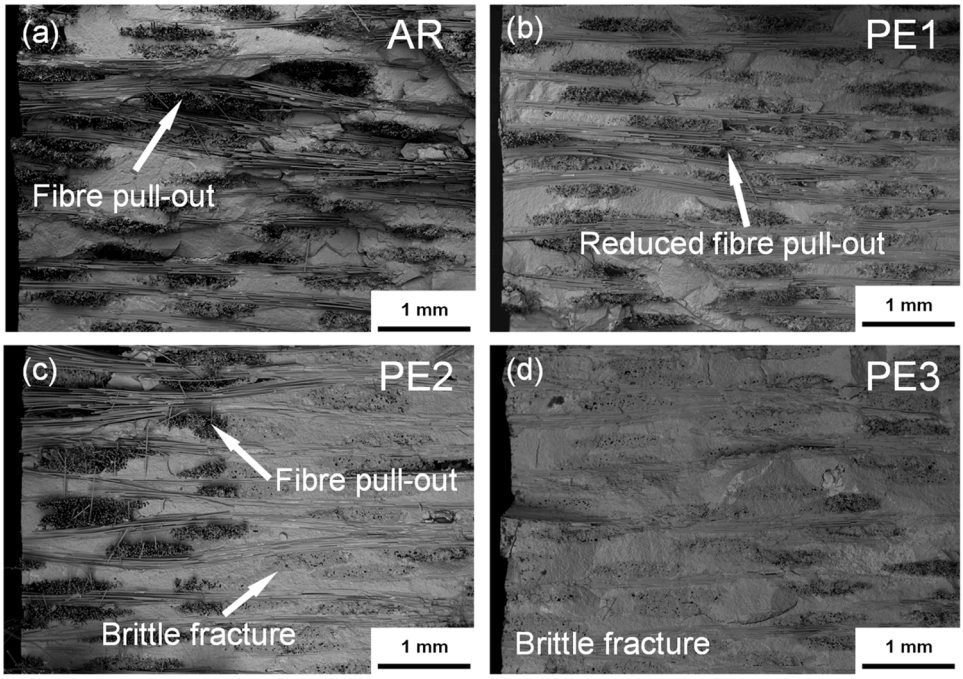

Fig. 17. Fracture surfaces for the tensile tested SiC_f/SiC CMC for the (a) as received (AR) material and for the different exposure conditions (b) PE1, (c) PE2 and (d) PE3.

Table 5
The mechanical and microwave sample properties due to environmental exposures relative to the as-received or pre-exposed CMC condition, with comments on the observed microstructural changes.

Sample	UTS (MPa)	Polarisation $-\Delta f/f_0$	Loss $\Delta(1/Q)$	Observed Microstructural Changes
AR (N = 9)	364	0.0229 ± 0.0001	0.0026 ± 0.0001	–
PE1 (N = 3 as for other PEs)	345	0.0233 ± 0.0001 2.4 ± 0.3 % increase	0.0031 ± 0.0002 28.0 ± 1 % increase	BN layer remains largely intact. Thick surface oxidation layer formed
PE2	133	0.0232 ± 0.0001 0.25 ± 0.04 % increase	0.0027 ± 0.0001 2.2 ± 0.2 % increase	Significant degradation of BN interphase. Si, B and N colocalised. Evidence of oxidation breaching the surface of the CMC towards the centre
PE3	43	0.0235 ± 0.0001 2.9 ± 0.1 % increase	0.0032 ± 0.0001 21.4 ± 0.4 % increase	Near complete depletion of BN interphase. Evidence of oxidation throughout the CMC

microwave characterisation, PE3 presented large changes in both polarisation and loss akin to those determined for PE1 which had the same time at 800 °C but no prior humidity exposure. However, while the polarisation change was very similar for PE1 and PE3 (2.4 % vs. 2.9 %, statistically insignificant via *t*-test), the loss change in PE3 (21.4 %) was less than that in PE1 (28.0 %), suggesting there is a mechanism that contributes to reducing loss in PE3. The key driver for the increase in dielectric loss is attributed to the formation of amorphous silica during oxidation of the SiC matrix, like that observed in PE1. Nonetheless, the volatilisation of the BN interphase in the PE3 condition has enabled routes for oxidation throughout the CMC including the SiC fibres, which is evidenced by the microstructure and fracture surface. It is the oxidation of the SiC fibres, which is accelerated in water vapour environments that is thought to lead to a reduction in their conductivity [39, 40], and thus a reduction in loss.

5. Conclusions

The research presented in this paper shows the development and investigation of the suitability for microwave cavity perturbation as a means for simple, non-invasive assessment of SiC_f/SiC CMC material. The method was successfully developed through a series of sensitivity, orientation and SiC fibre tow trials, that resulted in calibration curves for the measurement of polarisation and dielectric loss being determined through COMSOL modelling.

The developed technique was then applied to the same CMC material before and after it had been subjected to different environmental exposures that alter its microstructure, to determine whether shifts in microwave dielectric measurement could be attributed to microstructural changes. An increase in microwave dielectric measurements following the pre-exposures were attributed to oxidation, more specifically the formation of amorphous silica predominately at the surface of the CMC. Nonetheless, when a prior humidity exposure is applied before the same thermal exposure the increase in microwave dielectric loss is inhibited by the oxidation of the SiC fibres, and therefore their reduced conductivity, which is now possible due to the volatilisation of the BN interphase. Mechanical property changes following the pre-exposures were driven by the degradation of the BN interphase, which is a primary toughening phase with the CMC.

Future work will investigate the application of this method during mechanical testing, to understand whether it offers potential to understand and characterise damage progression in CMC material.

Data availability statement

The raw/processed data required to reproduce these findings cannot be shared at this time as the data also forms part of an ongoing study.

CRediT authorship contribution statement

Jordan Stephen: Methodology, Data curation, Writing – original

draft, Formal analysis, Writing – review & editing, Investigation, Conceptualization. **Spencer Jeffs:** Writing – review & editing, Project administration, Funding acquisition, Supervision, Investigation, Conceptualization, Writing – original draft, Methodology, Formal analysis. **Heungjae Choi:** Writing – original draft, Formal analysis, Writing – review & editing, Investigation, Conceptualization, Methodology, Data curation. **Adrian Porch:** Methodology, Data curation, Writing – original draft, Formal analysis, Writing – review & editing, Investigation, Conceptualization.

Declaration of competing interest

The authors declare the following financial interests/personal relationships which may be considered as potential competing interests:

Spencer Jeffs reports financial support was provided by Engineering and Physical Sciences Research Council. If there are other authors, they declare that they have no known competing financial interests or personal relationships that could have appeared to influence the work reported in this paper.

Acknowledgements

The current research was funded under the EPSRC Industrial Case Award EP/T517537/1. The provision of a research bursary, materials and supporting information from Rolls-Royce plc. is gratefully acknowledged. Mechanical testing was performed by Swansea Materials Research & Testing (SMaRT).

References

[1] J.A. DiCarlo, H.M. Yun, G.N. Morscher, R.T. Bhatt, SiC/SiC composites for 1200°C and above. Handbook of Ceramic Composites, Springer US, Boston, MA, 2005, pp. 77–98, https://doi.org/10.1007/0-387-23986-3_4.

[2] A. Gyekenyesi, Techniques for monitoring damage in ceramic matrix composites, J. Intell. Mater. Syst. Struct. 25 (13) (2014) 1531–1540, https://doi.org/10.1177/1045389X13510221. Sep.

[3] M.R. Bache, et al., Advances in damage monitoring techniques for the detection of failure in SiC_f/SiC ceramic matrix composites, Ceramics 2 (2) (2019) 347–371, https://doi.org/10.3390/ceramics2020028. May.

[4] F. Wang, et al., Damage and failure analysis of a SiCf/SiC ceramic matrix composite using digital image correlation and acoustic emission, Ceram. Int. 48 (4) (2022) 4699–4709, https://doi.org/10.1016/j.ceramint.2021.11.006. Feb.

[5] Y.P. Singh, M.J. Presby, M. Kannan, G.N. Morscher, Multi-lead direct current potential drop method for In situ health monitoring of ceramic matrix composites, J. Eng. Gas Turbines Power 141 (3) (2019) 1–10, https://doi.org/10.1115/1.4041271. Mar.

[6] G.N. Morscher, R. Maxwell, Monitoring tensile fatigue crack growth and fibre failure around a notch in laminate SIC/SIC composites utilizing acoustic emission, electrical resistance, and digital image correlation, J. Eur. Ceram. Soc. 39 (2–3) (2019) 229–239, https://doi.org/10.1016/j.jeurceramsoc.2018.08.049. Feb.

[7] Z. Quiney, S.P. Jeffs, L. Gale, S. Pattison, M.R. Bache, Matrix cracking onset stress and strain as a function of temperature, and characterisation of damage modes in SiC_f/SiC ceramic matrix composites via acoustic emission, J. Eur. Ceram. Soc. 43 (7) (2023) 2958–2967, https://doi.org/10.1016/j.jeurceramsoc.2022.10.042. Jul.

[8] Z. Quiney, E. Weston, P. Ian Nicholson, S. Pattison, M.R. Bache, Volumetric assessment of fatigue damage in a SiC_f/SiC ceramic matrix composite via in situ X-ray computed tomography, J. Eur. Ceram. Soc. 40 (11) (2020) 3788–3794, https://doi.org/10.1016/j.jeurceramsoc.2020.04.037Z. Sep.

[9] A. Morales-Rodríguez, P. Reynaud, G. Fantozzi, J. Adrien, E. Maire, Porosity analysis of long-fibre-reinforced ceramic matrix composites using X-ray tomography, Scr. Mater. 60 (6) (2009) 388–390, https://doi.org/10.1016/j.scriptamat.2008.11.018.

[10] S.P. Jeffs, J. Stephen, Z. Quiney, G.García Luna, Vibration and acoustic emission assessment of a SiC_f/SiC ceramic matrix composite with damage, in: Proceedings of the ASME Turbo Expo2024: Turbomachinery Technical Conference and Exposition, London, United Kingdom, ASME, 2024, https://doi.org/10.1115/GT2024-127571. June 24–28V002T02A014.

[11] V. Kostopoulos, Y.Z. Pappas, Y.P. Markopoulos, Fatigue damage accumulation in 3-dimensional SiC/SiC composites, J. Eur. Ceram. Soc. 19 (1999) 207–215.

[12] Z. Yang, C. Pei, H. Yan, L. Long, Fatigue damage modeling of ceramic-matrix composites: a short review, Mater. Des. Process. Commun. 2 (2) (2020) 1–8, https://doi.org/10.1002/mdp2.129. Apr.

[13] M.Y. He, B.X. Wu, A.G. Evans, J.W. Hutchinson, Inelastic strains due to matrix cracking in unidirectional fibre-reinforced composites, Mech. Mater. 18 (3) (1994) 213–229, https://doi.org/10.1016/0167-6636(94)90022-1. Aug.

[14] A.G. Evans, F.W. Zok, R.M. McMeeking, Fatigue of ceramic matrix composites, Acta Metall. Mater. 43 (3) (1995) 859–875, https://doi.org/10.1016/0956-7151(94)00304-Z. Mar.

[15] B.W. Sheldon, E.Y. Sun, S.R. Nutt, J.J. Brennan, Oxidation of BN-coated SiC fibres in ceramic matrix composites, J. Am. Ceram. Soc. 79 (2) (1996) 539–543, https://doi.org/10.1111/j.1151-2916.1996.tb08163.x. Feb.

[16] E.J. Opila, N.S. Jacobson, Oxidation and corrosion of ceramics, in: Ceramics Science and Technology, 4, Wiley-VCH Verlag GmbH & Co. KGaA, Weinheim, Germany, 2013, pp. 1–93, https://doi.org/10.1002/9783527631971.ch01.

[17] S. Guo, T. Mamiya, Y. Kagawa, In situ nondestructive evaluation of the accumulative damage in continuous ceramic fibre-ceramic matrix composites (CFCCs) using submillimeter range electromagnetic wave, Adv. Eng. Mater. 6 (8) (2004) 681–683, https://doi.org/10.1002/adem.200400033.

[18] R. Raihan, J.M. Adkins, J. Baker, F. Rabbi, K. Reifsnider, Relationship of dielectric property change to composite material state degradation, Compos. Sci. Technol. 105 (2014) 160–165, https://doi.org/10.1016/j.compscitech.2014.09.017.

[19] S. Guo, Y. Kagawa, Relationships between the accumulative damage and dielectric properties of woven BN-coated Hi-Nicalon™ SiC fibre-reinforced SiC matrix composites, Ceram. Int. 41 (6) (2015) 7366–7373, https://doi.org/10.1016/j.ceramint.2015.02.043.

[20] A.W. Kraszewski, S.O. Nelson, Resonant cavity perturbation - some new applications of an old measuring technique, J. Microw. Power Electromagn. Energy 31 (3) (1996) 178–187, https://doi.org/10.1080/08327823.1996.11688308.

[21] O.G. Diaz, et al., Degradation mechanisms of SiC/BN/SiC after low temperature humidity exposure, J. Eur. Ceram. Soc. 40 (12) (2020) 3863–3874, https://doi.org/10.1016/j.jeurceramsoc.2020.05.007. Sep.

[22] G.S. Corman, K.L. Luthra, Silicon melt infiltrated ceramic composites (HiPerComp™. Handbook of Ceramic Composites, Springer US, 2006, pp. 99–115, https://doi.org/10.1007/0-387-23986-3_5.

[23] M. Barter, G. Smith, S. Yang, M. Schröder, M.O. Jones, A. Porch, Simultaneous neutron powder diffraction and microwave characterisation at elevated temperatures, Phys. Chem. Chem. Phys. 23 (41) (2021) 23602–23609, https://doi.org/10.1039/d1cp03658k.

[24] J.A. Cuenca, et al., Microwave permittivity of trace sp(2) carbon impurities in submicron diamond powders, ACS Omega 3 (2) (2018) 2183–2192, https://doi.org/10.1021/acsomega.7b02000. Feb.

[25] D. Rauch, M. Dietrich, T. Simons, U. Simon, A. Porch, R. Moos, Microwave cavity perturbation studies on H-form and Cu ion-exchanged SCR catalyst materials: correlation of ammonia storage and dielectric properties, Top. Catal. 60 (3–5) (2016) 243–249, https://doi.org/10.1007/s11244-016-0605-z.

[26] D.M. Pozar, Microwave Engineering, 4th ed., John Wiley & Sons, New York, 2011.

[27] D. Kajfez, E.J. Hwan, Q-factor measurement with network analyzer, IEEE Trans. Microw. Theory Tech. 32 (7) (1984) 666–670, https://doi.org/10.1109/tmtt.1984.1132751.

[28] O. Klein, S. Donovan, M. Dressel, G. Grüner, Microwave cavity perturbation technique: part I: principles, J. Infrared Millim. Terahertz Waves 14 (12) (1993) 2423–2457, https://doi.org/10.1007/bf02086216.

[29] A.A. Abduljabar, X. Yang, D.A. Barrow, A. Porch, Modelling and measurements of the microwave dielectric properties of microspheres, IEEE Trans. Microw. Theory Tech. 63 (12) (2015) 4492–4500, https://doi.org/10.1109/tmtt.2015.2495247.

[30] I. Kuzmanić, I. Vujović, M. Petković, J. Šoda, Influence of 3D printing properties on relative dielectric constant in PLA and ABS materials, Prog. Addit. Manuf. 8 (4) (2023) 703–710, https://doi.org/10.1007/s40964-023-00411-0. Aug.

[31] Y. Katoh, S. Kondo, L.L. Snead, DC electrical conductivity of silicon carbide ceramics and composites for flow channel insert applications, J. Nucl. Mater. 386–388 (2009) 639–642, https://doi.org/10.1016/j.jnucmat.2008.12.237.

[32] R. Scholz, F. dos Santos Marques, B. Riccardi, Electrical conductivity of silicon carbide composites and fibres, J. Nucl. Mater. 307–311 (2002) 1098–1101, https://doi.org/10.1016/s0022-3115(02)00950-9.

[33] K.N. Detwiler, E.J. Opila, Oxidation of SiC/BN/SiC ceramic matrix composites in dry and wet oxygen at intermediate temperatures, J. Eur. Ceram. Soc. 42 (10) (2022) 4110–4120, https://doi.org/10.1016/j.jeurceramsoc.2022.04.003. Aug.

[34] E.J. Opila, R.C. Robinson, M.J. Verrilli, Borosilicate glass-induced fibre degradation of SiC/BN/SiC composites exposed in combustion environments, Int. J. Appl. Ceram. Technol. 13 (3) (2016) 434–442, https://doi.org/10.1111/ijac.12499. May.

[35] W.D. Oliver, P.B. Welander, Materials in superconducting quantum bits, MRS Bull. 38 (10) (2013) 816–825, https://doi.org/10.1557/mrs.2013.229. Oct.

[36] A. Saeed, S.O. Adewuyi, H.A.M. Ahmed, S.R. Alharbi, S.E. Al Garni, F. Abolaban, Electrical and dielectric properties of the natural calcite and quartz, Silicon 14 (2022) 5265–5276, https://doi.org/10.1007/s12633-021-01318-7/Published.

[37] M. Naftaly, A. Gregory, Terahertz and microwave optical properties of single-crystal quartz and vitreous silica and the behavior of the boson peak, Appl. Sci. 11 (6733) (2021), https://doi.org/10.3390/app11156733. Aug.

[38] G.N. Morscher, J. Hurst, D. Brewer, Intermediate-temperature stress rupture of a woven hi-nicalon, BN-interphase, SiC-matrix composite in air, J. Am. Ceram. Soc. 83 (6) (2000) 1441–1449, https://doi.org/10.1111/j.1151-2916.2000.tb01408.x. Jun.

[39] R. Scholz, F. Dos, S. Marques, B. Riccardi, Electrical conductivity of silicon carbide composites and fibres, J. Nucl. Mater. 307–311 (2002) 1098–1101.

[40] Z. Li, X. Zhang, Q. Zhang, E. Avcu, P.J. Withers, P. Xiao, Oxidation and mechanical properties of SiC fibres after high temperature exposure in air and steam, J. Eur. Ceram. Soc. 44 (12) (2024) 6864–6874, https://doi.org/10.1016/j.jeurceramsoc.2024.04.076. Sep.